Inorganic Chemistry

pubs.acs.org/IC

Article

High-Pressure Synthesis of Two Polymorphic $HgMnO_3$ Phases and Distinct Magnetism from 2D to 3D

Bowen Zhou, Shijun Qin, Teng Ma, Xubin Ye, Jia Guo, Xiaohui Yu, Hong-Ji Lin, Chien-Te Chen, Zhiwei Hu, Liu-Hao Tjeng, Guanghui Zhou, Cheng Dong, and Youwen Long*

Cite This: *Inorg. Chem.* 2020, 59, 3887−3893

Read Online

ABSTRACT: An ilmenite-like monoclinic phase of $HgMnO_3$ with space group $P2_1/c$ was prepared using high-pressure and high-temperature methods at 18 GPa and 1473 K. The MnO_6 octahedra form a two-dimensional (2D) network in the *bc* plane, leading to a long-range antiferromagnetic ordering with a low Néel temperature of $T_N \sim 32$ K. As the synthesis pressure increases to 20 GPa, a new perovskite-like rhombohedral phase with space group $R\bar{3}c$ was found to occur. The rhombohedral phase exhibits a three-dimensional (3D) network for the MnO_6 octahedra, giving rise to an antiferromagnetic ordering at $T_N \sim 60$ K. X-ray absorption spectroscopy confirms the invariable Mn^{4+} charge state in these two polymorphic phases, in agreement with the Curie−Weiss and bond valence sum analysis. $HgMnO_3$ provides an interesting example to study the magnetic properties from 2D to 3D by varying synthesis pressure.

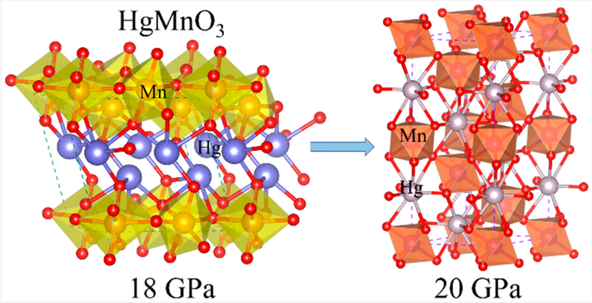

■ INTRODUCTION

Manganese perovskite oxides have received much attention owing to their intriguing physical properties like colossal magnetoresistance effects, charge, spin and orbital orderings, as well as magnetoelectric multiferroicity.[1−8] As far as the $A^{2+}Mn^{4+}O_3$ perovskite family is concerned, when a larger A-site ion such as Sr^{2+}, Ba^{2+}, or Pb^{2+} is involved, a wide variety of polymorphic structures can be formed at different synthesis conditions, which significantly affects the magnetic and electronic properties. As shown in Figure 1, the 6H-, 4H-, and C-type $SrMnO_3$ (H and C stand for hexagonal and cubic structures, respectively) occur at different synthesis pressures with the antiferromagnetic Néel temperature $T_N \sim 235$, 280, and 240 K, respectively.[9,10] Similarly, with increasing synthesis pressure, the crystal structure of $BaMnO_3$ changes from 2H to 4H via an intermediate 9R phase (R stands for a rhombohedral structure) due to the stacking mode alteration of the hexagonal close-packed structures.[11−13] In addition, $PbMnO_3$ crystallizes into a 6H phase at 8 GPa while it changes to a 3C phase at 15 GPa.[14] On the other hand, when the A-site of the $A^{2+}Mn^{4+}O_3$ family is occupied by a smaller cation like Ca^{2+}, a distorted orthorhombic perovskite structure is found to occur in $CaMnO_3$ with corner-sharing MnO_6 octahedra in space.[15,16] Further reducing the A-site size will change the perovskite structure to an ilmenite phase, as observed in $MgMnO_3$ with layered MnO_6 octahedral network.[17]

In comparison, the effective ionic radius of Hg^{2+} is close to that of Ca^{2+}.[18] However, because of the strong volatility of

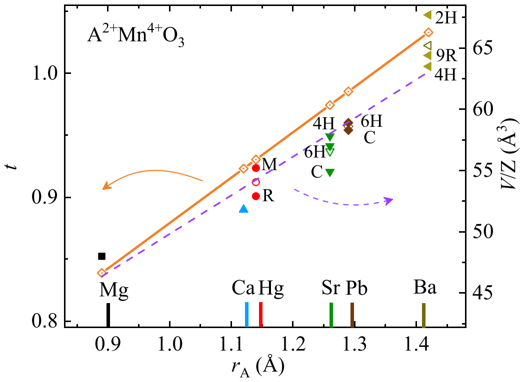

Figure 1. Tolerance factor (t) and unit cell volume normalized for each formula unit (V/Z) and as a function of A-site cation radius for $A^{2+}Mn^{4+}O_3$ (A = Mg, Hg, Ca, Sr, Pb, Ba) family. M, R, C, and H stand for monoclinic, rhombohedral, cubic, and hexagonal crystal structures, respectively. Different crystal phases are shown for A = Hg, Sr, Pb, Ba. The dashed line is a linear fit for the average V/Z (open symbols) for different members.

Received: December 6, 2019
Published: March 3, 2020

https://dx.doi.org/10.1021/acs.inorgchem.9b03551

HgO on heating, $HgMnO_3$ has never been prepared as yet. Benefiting from the enclosed reaction environment, high-pressure synthesis is an effective method to suppress element volatilization. As a result, some stoichiometric mercury oxides such as $HgTiO_3$[19] and $HgPbO_3$[20] were obtained under high pressure. Moreover, high pressure can remarkably reduce the A-site ionic size as well as the octahedral distortions. Therefore, if $HgMnO_3$ can be prepared under high-pressure and high-temperature conditions, it may crystallize into an ilmenite- or perovskite-like structure at different synthesis conditions, as observed in $PbNiO_3$.[21] Since the MnO_6 octahedra have essentially different arrangements in the ilmenite and perovskite structures (2D vs 3D),[15,17] distinct magnetic properties are expected to occur in these two phases.

In this work, we have succeeded in the preparation of two polymorphic phases of $HgMnO_3$ with different magnetic dimensionalities. An ilmenite-like monoclinic $HgMnO_3$ (M-HMO) is obtained at a pressure of 18 GPa. This phase exhibits 2D magnetic behavior. Interestingly, once the synthesis pressure is increased only by 2 GPa (i.e., up to 20 GPa), a new perovskite-like rhombohedral $HgMnO_3$ (R-HMO) is formed. In sharp contrast to the 2D magnetism of the ilmenite phase, the perovskite phase shows 3D magnetic properties.

■ EXPERIMENTAL SECTION

Highly pure (>99.9%) HgO and MnO_2 powders at an 1:1 mol ratio were used as starting materials to prepare the two polymorphic phases of $HgMnO_3$. Since HgO was highly toxic, the starting materials were thoroughly mixed using an agate mortar and then sealed into Au capsules in a glovebox filling with nitrogen gas. The Au capsules with a 2.0 mm diameter and height were treated on a Walker-type double-stage high-pressure apparatus. The M-HMO was prepared at 18 GPa and 1473 K for 30 min. Identical temperature and time conditions were adopted to synthesize the R-HMO while the pressure was set at 20 GPa. Powder X-ray diffraction (XRD) was measured using a Huber diffractometer with Cu $K\alpha_1$ radiation in the 2θ range from 10° to 100° at room temperature (RT) with steps of 0.005°. The primary crystal structures were resolved by EXPO2014 program[22] from the powder diffraction data. Then, the Rietveld refinements for the XRD data were performed using the FullProf program.[23] X-ray absorption spectroscopy (XAS) at the Mn$-L_{2,3}$ edges was measured at the BL11A beamline of NSRRC using the total electron yield mode at RT. Magnetic susceptibility and magnetization measurements were carried out using a superconducting quantum interference device magnetometer (Quantum Design, MPMS-VSM). Specific heat (C_p) data were collected on a physical property measurement system (Quantum Design, PPMS-9T) using a pulse relaxation method at zero magnetic field.

■ RESULTS AND DISCUSSION

Figure 2a presents the room-temperature XRD pattern of $HgMnO_3$ prepared at 18 GPa as well as the Rietveld structural refinement results. To resolve the crystal structure, we first tried to search isostructural references. Unfortunately, however, no satisfied isostructural model was found to our knowledge. We therefore turned to the direct method to obtain primary structural parameters like possible space groups, lattice constants, and atomic positions by using the EXPO2014 program.[22] Then, the Rietveld refinements were carried out based on the primary structural information determined from the direct method. By comparing the satisfactory factors R_p and R_{wp}, the most reliable structure model was assigned. In our analysis, the XRD data presented in Figure 2a can be best fitted on the basis of an ilmenite-like monoclinic structure model with a centrosymmetric space group $P2_1/c$ (no. 14). In this crystal symmetry, the Hg and Mn atoms both occupy a special Wyckoff position 4*e* (*x*, *y*, *z*), while the O occupies three different 4*e* sites. Table 1 lists the refined structural parameters of M-HMO including the detailed atomic positions, bond lengths, and angles. The obtained lattice parameters are a = 6.72149(6) Å, b = 4.97673(4) Å, c = 6.88710(5) Å, and β = 106.2745(5)°. As shown in Figure 2b, each Mn is coordinated by six ligand O atoms with the Mn−O distance varying from 1.87 to 2.04 Å, forming a MnO_6 octahedron. The MnO_6 octahedra are connected to each other by sharing corners along the *c*-axis. Along the *a*-axis, however, the octahedra are spatially separated by nonmagnetic Hg atoms. The magnetic MnO_6 octahedra thus form a 2D network in *bc* plane (see Figure 2b). Note that during the structural analysis, a small amount of MnO_2 (4.94 wt %) and HgO (0.78 wt %) impurity phases are discernible as shown in Figure 2a, but they do not affect the intrinsic magnetism of $HgMnO_3$ as shown later.

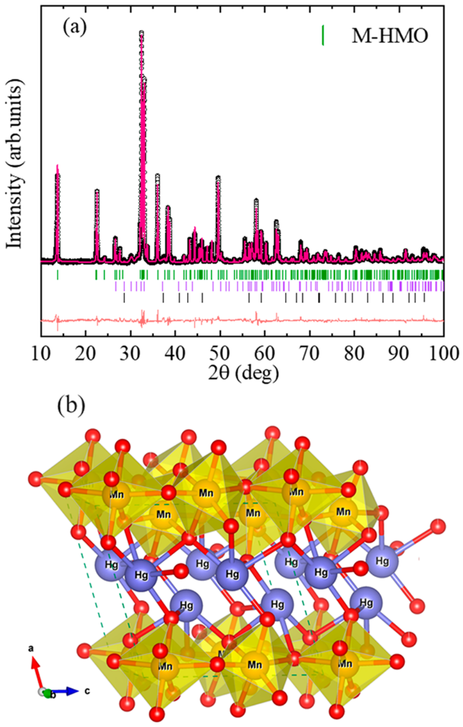

Figure 2. (a) XRD pattern and the Rietveld refinement results of M-HMO at RT. The observed (dots), calculated (red line), and difference (orange line) are shown. The top ticks indicate the allowed Bragg reflections with space group $P2_1/c$. The middle and bottom ticks present a small amount of HgO [4.94(5) wt %] and MnO_2 [0.78(2) wt %] impurity phases. (b) Schematic crystal structure of M-HMO with layered MnO_6 octahedral distribution in *bc* plane.

Figure 3a shows the room-temperature XRD pattern and the Rietveld refinement results for $HgMnO_3$ prepared at 20 GPa. Compared with the M-HMO, the XRD pattern changes essentially, indicating the occurrence of a new crystal structure. Similar structural analysis procedure with that applied for the M-HMO was performed for the new phase. The detailed analysis demonstrates that, except for the minor MnO_2 and HgO impurities, all the main diffraction peaks of the new phase can be best fitted using a perovskite-like rhombohedral structure model with space group $R\bar{3}c$ (no. 167) or its subgroup $R3c$ (no. 161). Since lowering symmetry from $R\bar{3}c$ to $R3c$ leads to unreasonably large error bars for atomic positions and cannot significantly reduce the R_p and R_{wp} factors, the

Table 1. Refined Crystallographic Parameters for the Monoclinic $HgMnO_3$ ($Z = 4$).[a]

parameter	value	parameter	value	parameter	value
Hg_x	0.60537(7)	***B*** for Hg ($Å^2$)	0.28(2)	Mn−O1 (Å)	1.869(7)
Hg_y	0.2311(2)	***B*** for Mn ($Å^2$)	0.82(7)	Mn−O2 (Å)	1.954(8)
Hg_z	0.11145(7)	***B*** for O1 ($Å^2$)	1.3(3)	Mn−O2 (Å)	1.916(7)
Mn_x	0.0756(3)	***B*** for O2 ($Å^2$)	0.7(3)	Mn−O3 (Å)	2.043(9)
Mn_y	0.256(9)	***B*** for O3 ($Å^2$)	0.9(3)	Mn−O3 (Å)	1.929(8)
Mn_z	0.0983(3)	***G*** for Hg	1.00(1)	Mn−O3 (Å)	2.032(9)
$O1_x$	0.347(1)	***G*** for Mn	0.99(1)	Mn−O2−Mn (deg)	94.0(4)
$O1_y$	0.146(2)	Hg−O1 (Å)	2.127(8)	Mn−O3−Mn (deg)	128.3(4)
$O1_z$	0.223(1)	Hg−O1 (Å)	2.338(8)	Mn−O3−Mn (deg)	115.4(4)
$O2_x$	0.190(1)	Hg−O2 (Å)	2.476(7)	Mn−O3−Mn (deg)	95.4(5)
$O2_y$	0.600(1)	Hg−O2 (Å)	2.140(8)	BVS (Hg)	2.55(2)
$O2_z$	0.044(1)	Hg−O3 (Å)	2.350(8)	BVS (Mn)	3.58(3)
$O3_x$	0.098(1)				
$O3_y$	0.467(1)				
$O3_z$	0.358(1)				

[a] Space group $P2_1/c$ (no. 14); atomic sites are Hg 4e, Mn 4e, O1 4e, O2 4e, and O3 4e; $a = 6.72149(6)$ Å, $b = 4.97673(4)$ Å, $c = 6.88710(5)$ Å, $\beta = 106.2745(5)°$, $V = 221.146(4)$ $Å^3$; $R_{wp} = 4.35\%$, $R_p = 3.25\%$. The calculated density $\rho = 9.111$ g/cm^3. B is the isotropic temperature factor. The occupation factor G for oxygen is fixed to 1. BVS values (V_i) were calculated using the formula $V_i = \sum_j S_{ij}$, $S_{ij} = \exp[(r_0 - r_{ij})/0.37]$, $r_0(Mn^{4+}) = 1.753$ Å, $r_0(Hg^{2+}) = 1.972$ Å.[36]

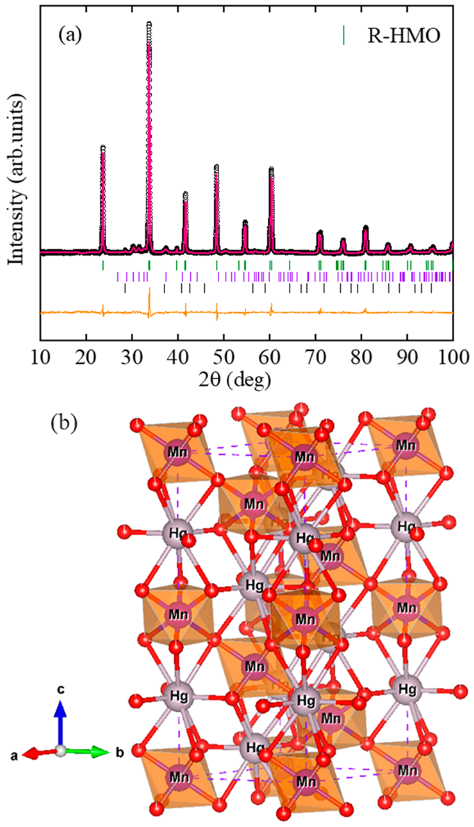

Figure 3. (a) XRD pattern and the Rietveld refinement results of R-HMO at RT. The observed (dots), calculated (red line), and difference (orange line) are shown. The top ticks indicate the allowed Bragg reflections with space group $R\overline{3}c$. The middle and bottom ticks present a small amount of HgO [7.8(1) wt %] and MnO_2 [5.22(1) wt %] impurity phases. (b) Schematic crystal structure of R-HMO with corner-sharing MnO_6 octahedral distribution in space.

Table 2. Refined Crystallographic Parameters for the Rhombohedral $HgMnO_3$ ($Z = 6$)[b]

parameter	value	parameter	value
O_x	0.4202(6)	Hg−O (Å) × 2	2.6943(5)
B for Hg ($Å^2$)	0.17(2)	Hg−O (Å) × 2	2.694(1)
B for Mn ($Å^2$)	0.54(6)	Mn−O (Å) × 2	1.925(3)
B for O ($Å^2$)	0.2(2)	Mn−O (Å) × 2	1.9249(7)
G for Hg	1.02(1)	Mn−O (Å) × 2	1.925(2)
G for Mn	1.03(1)	Mn−O−Mn (deg) × 6	154.6(2)
Hg−O (Å)	2.228(4)	BVS (Hg)	2.202(5)
Hg−O (Å) × 2	2.228(2)	BVS (Mn)	3.803(8)
Hg−O (Å) × 2	2.694(2)		

[b] Space group $R\overline{3}c$ (no. 167); atomic sites are Hg 6a (0, 0, 0.25), Mn 6b (0, 0, 0), and O 18e (x, 0, 0.25); $a = 5.30116(8)$ Å, $c = 13.0612(2)$ Å, $V = 317.857(8)$ $Å^3$; $R_{wp} = 3.33\%$, $R_p = 1.94\%$. B is the isotropic temperature factor. The occupation factor G for oxygen is fixed to 1. The calculated density $\rho = 9.501$ g/cm^3. BVS calculation methods are the same as mentioned in Table 1.

higher symmetrical $R\overline{3}c$ was assigned to the higher-pressure phase of $HgMnO_3$. In this structural framework, the Hg is located at a special Wyckoff site 6*a* (0, 0, 0.25), Mn at 6*b* (0, 0, 0), and O at 18*e* (x, 0, 0.25). As listed in Table 2, the refined lattice parameters are $a = 5.30116(8)$ and $c = 13.0612(2)$ Å. Along with the structure phase transition from the lower-pressure ilmenite phase to the higher-pressure perovskite phase, the cell volume normalized for each chemical formula is reduced by about 4.28%, indicating that the R-HMO is a higher-density phase, as expected from the higher synthesis pressure for this phase. If one compares the ligand atom number for Hg and Mn, it is found that the coordinated O atoms increase from 5 to 9 for Hg with the Hg−O distance varying from 2.12 to 2.82 Å during the structural phase transformation. However, the Mn always possesses a MnO_6 octahedral coordination. In the R-HMO, all the MnO_6 octahedra are corner-sharing with each other, forming a 3D arrangement in space (see Figure 3b). According to the refined Hg−O and Mn−O bond lengths, we performed bond valence sum calculations for the Hg and Mn. As shown in Tables 1 and 2, the valence state of Mn in both phases is close to +4, while the valence state of Hg is a little larger than +2 due to the overbonding effect caused by high-pressure synthesis.

To further determine the valence state for the transition-metal Mn, we have collected soft XAS spectra at the Mn-$L_{2,3}$

https://dx.doi.org/10.1021/acs.inorgchem.9b03551
Inorg. Chem. 2020, 59, 3887−3893

edges, which are well-known to be sensitive to the valence state and the local environment of 3d transition metal ions in solid oxides.[24−27] Figure 4 shows the Mn-$L_{2,3}$ edges of both M- and R-HMO together with the Mn^{4+} reference $SrMn^{4+}O_3$[24] and the Mn^{3+} reference $LaMn^{3+}O_3$[24] with similar MnO_6 octahedral coordination. Compared with the $LaMnO_3$, the absorption spectra of both M- and R-HMO shift toward higher energies by about 1.3 eV, suggesting a higher Mn valence state than +3 in $HgMnO_3$. By comparison, these two polymorphic phases display very similar spectral features such as the peak profile and energy positions with those of the Mn^{4+} reference $SrMnO_3$, confirming the formation of Mn^{4+} charge state as well as the oxygen stoichiometricity. Therefore, the same magnetic ions of Mn^{4+} exist in the monoclinic and hexagonal $HgMnO_3$. However, since the MnO_6 units are arranged differently in these two phases (2D vs 3D), it is very interesting to study the magnetic variation in both phases.

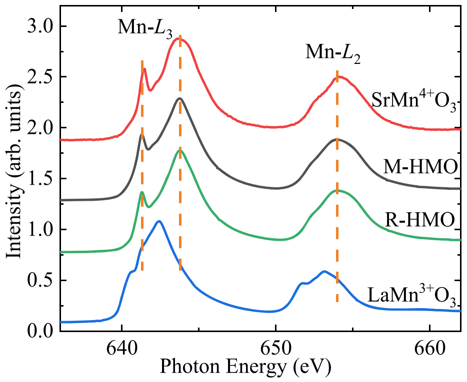

Figure 4. X-ray absorption spectra at the Mn-$L_{2,3}$ edges for M-HMO and R-HMO together with related reference compounds $LaMnO_3$ and $SrMnO_3$ for comparison.

Figure 5a presents the temperature dependence of the zero-field-cooling (ZFC) and field-cooling (FC) magnetic susceptibility curves for the M-HMO measured at 0.1 T. The susceptibility smoothly increases with decreasing temperature and forms a broad hump at around 60 K. This feature is reminiscent of layered 2D Heisenberg antiferromagnets as observed in, for example, $MnPS_3$.[28] The interlayer short-range spin interactions of the Mn^{4+} ions are responsible for the formation of this broad hump. Below 60 K, the susceptibility starts to decrease and experiences a drastic drop at $T_N \sim 32$ K. If one takes the derivative of the susceptibility as a function of temperature, a sharp peak can be found at T_N (see the inset of Figure 5a). Moreover, a λ-type anomaly is also observed around T_N in specific heat (shown later). These observations reveal a long-range antiferromagnetic phase transition induced by intralayer Mn^{4+}−O−Mn^{4+} superexchange interactions in the *bc* plane. Above 175 K, the inverse susceptibility data can be well fitted based on the Curie−Weiss law, yielding a Curie constant C = 1.7215(8) emu·K·mol^{-1}·Oe^{1-}, and a Weiss temperature $\theta = -31.0(1)$ K. The negative sign of θ agrees with the antiferromagnetic ordering, and the absolute value of θ is comparable with the T_N mentioned above. According to the Curie constant, we calculated the effective magnetic moment $\mu_{eff} = 3.71\ \mu_B$/f.u. This value is very close to the spin-only theoretical one for a Mn^{4+} ion (3.87 μ_B/f.u.). The M-HMO shows also a very strong insulating behavior with a resistivity larger than 10^5 ohm·cm at RT (not shown here). These observations indicate that the M-HMO is an antiferromagnetic Mott insulator. As shown in Figure 5a, the ZFC and FC magnetic susceptibility curves of M-HMO overlap completely, suggesting that there is no spin-canting-induced net magnetic moment. This is in good agreement with the linear magnetization behavior without any discernible magnetic hysteresis measured below and above T_N, as shown in Figure 5b. Note that although a small amount of magnetic impurity phase of MnO_2 is observed during the structural refinement, one cannot find any magnetic anomaly at its Néel temperature of 92 K,[29] indicating the negligible effect on the intrinsic magnetism of M-HMO.

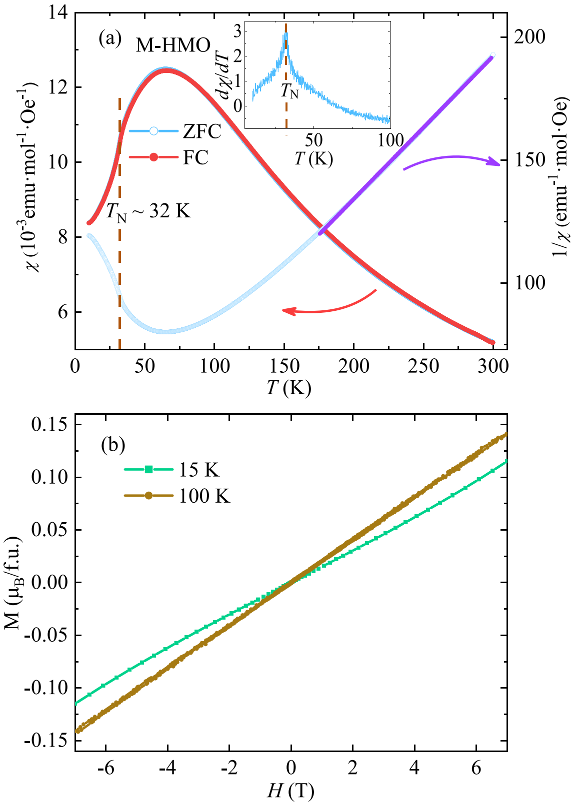

Figure 5. (a) Temperature-dependent magnetic susceptibility and inverse magnetic susceptibility measured at 0.1 T for M-HMO. The purple line between 175 and 300 K shows the Curie−Weiss law fitting with the function $\chi^{-1} = (T - \theta)/C$. The inset shows the derivative of susceptibility. (b) Field-dependent magnetization measured at different temperatures.

The magnetic properties of R-HMO are characterized by the same measurements as those performed on the M-HMO. Figure 6 shows the magnetic susceptibility and magnetization curves of R-HMO. Different from the broad hump observed in the 2D antiferromagnet M-HMO, the 3D R-HMO exhibits a sharp antiferromagnetic phase transition at $T_N \sim 60$ K (Figure 6a). The magnetic susceptibility data above 125 K also follow the Curie−Weiss law. The fitting gives C = 2.533(2) emu·K·mol^{-1}·Oe^{1-} and $\theta = -153.6(3)$ K. The absolute value of θ obtained in the R-HMO is much larger than that of M-HMO, suggesting stronger antiferromagnetic interactions in the 3D HMO phase. Based on the Curie constant, the effective magnetic moment was calculated to be 4.50 μ_B/f.u. This value is slight larger than that fitted for the M-HMO (3.71 μ_B/f.u.) but is very similar to those reported in the isoelectronic compounds $CaMnO_3$ (4.34 μ_B/f.u.)[30] and 4H-$SrMnO_3$ (4.6

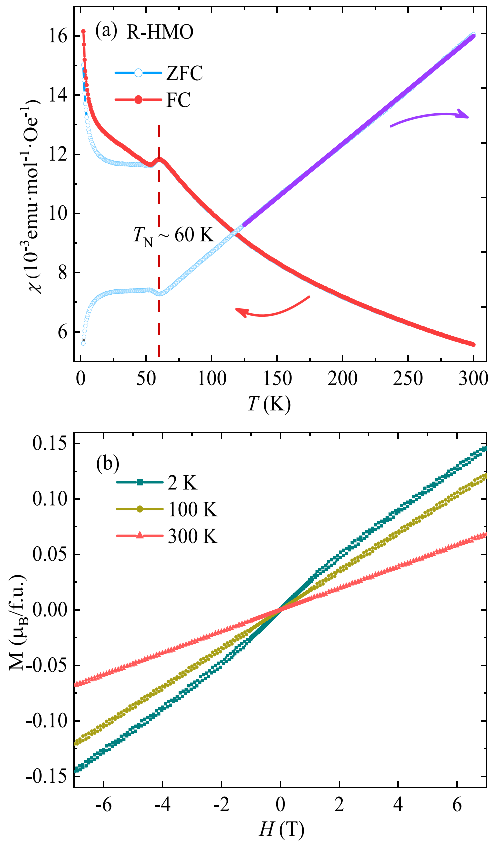

Figure 6. (a) Temperature-dependent magnetic susceptibility and inverse magnetic susceptibility measured at 0.1 T for R-HMO. The purple line between 125 and 300 K shows the Curie−Weiss law fitting. (b) Field-dependent magnetization measured at different temperatures.

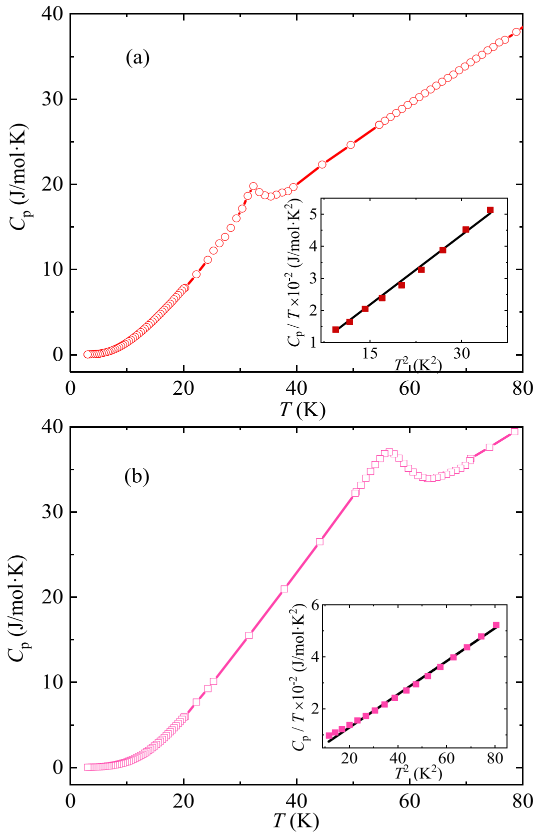

Figure 7. Temperature dependence of specific heat for (a) M-HMO and (b) R-HMO below 80 K at zero field. The insets show linear fitting results using the formula $C_p/T = \beta T^2$, giving β = 1.45 mJ/mol·K^4 for M-HMO, and 0.64 mJ/mol·K^4 for R-HMO.

μ_B/f.u.).[11] At lower temperatures, the ZFC and FC curves of R-HMO separate a little, probably implying a noncollinear antiferromagnetic structure due to slight spin canting. Similar behaviors are observed in $PbMnO_3$[14] and $SrMnO_3$.[9] Figure 6b shows the isothermal magnetization curves of R-HMO measured at different temperatures. Above T_N, the linear magnetization is coherent with the paramagnetism. At 2 K, however, a small amount of magnetic hysteresis is found to occur, in agreement with the possible spin canting mentioned above. Again, the magnetic impurity phase of MnO_2 also has no detectable effect on the intrinsic magnetism of R-HMO. As a matter of fact, all the other members in the $A^{2+}Mn^{4+}O_3$ (A = Mg, Hg, Ca, Sr, Pb, Ba) family also show antiferromagnetic ground states.

Figure 7 presents the temperature-dependent specific heat C_p measured at zero field for the M-HMO and R-HMO. Although the magnetic susceptibility of M-HMO experiences a broad hump around 60 K, no anomaly is found to occur in C_p, revealing that the interlayer antiferromagnetic interactions are short ranged around this temperature. At lower temperatures, a sharp λ-type anomaly is observed in the specific heat at T_N ~ 32 K (Figure 7a), confirming the long-range antiferromagnetic phase transition caused by the intralayer superexchange interactions. Similarly, corresponding to the long-range antiferromagnetic ordering of R-HMO, a sharp specific heat anomaly is also found to occur at T_N ~ 60 K (Figure 7b). Due to the strong insulating behavior as well as the antiferromagnetic coupling, the low-temperature C_p/T data of both M- and R-HMO follow a T^2 relationship (i.e., $C_p/T = \beta T^2$). As shown in the insets of Figure 7, the C_p/T and T^2 data display good linear behaviors for these two polymorphic phases at lower temperatures. It means that antiferromagnetic excitations and phonons both dominate the specific heat.

The Goldschmidt's tolerance factor $t = (r_A + r_O)/\sqrt{2}(r_B + r_O)$ is often used to predict ABO_3 perovskite structures.[31−34] Here, r_A, r_B, and r_O stand for effective ionic radii for A, B, and O ions, respectively. The value of $t = 1$ corresponds to an ideal cubic perovskite structure while $t < 1$ leads to cooperative octahedral distortions with reduced crystal symmetry due to a smaller A-site ionic size. Further lowering the A-site size can change the perovskite structure to an ilmenite-type one.[35] On the other hand, for a larger A-site atom like Pb or Ba with $t > 1$, complex polytypes with different kinds of hexagonal stacking can be formed to reduce the Madelung energy. As shown in Figure 1, as the whole family of $A^{2+}Mn^{4+}O_3$ with A = Mg, Hg, Ca, Sr, Pb, and Ba is concerned, the tolerance factor exhibits a good linear relationship with the ionic radius, although the end member of $MgMnO_3$ has an ilmenite structure. Moreover, the average unit cell volume per chemical formula for each member also approximately follows a linear relationship with the ionic size. By comparison the A-site size of $A^{2+}Mn^{4+}O_3$ family as summarized in Figure 1, the size of Hg^{2+} is located at the region of perovskite phase. However, the lower-pressure phase of $HgMnO_3$ crystallizes into an ilmenite-like structure, suggesting that, in addition to the A-site ionic size, there exist other factors affecting the phase stability. In sharp contrast to the outermost empty d-orbitals of the family members with A

= Mg, Ca, Sr and Ba, the outermost 5d orbitals of Hg^{2+} are fully occupied, which may give rise to different chemical reaction activities. The detailed electronic configurations of A-site ions are thus probable to play a role for the phase stability in $A^{2+}Mn^{4+}O_3$ family. During the synthesis of $HgMnO_3$ in this work, we tried various synthesis pressures like 6, 8, and 15 GPa at 1373−1473 K. However, the starting materials do not take mutually chemical reaction at 6 and 8 GPa. Even at 15 GPa, only a small amount of M-HMO phase is found to occur in the product. As the pressure increases to 18 GPa, however, one can obtain a nearly single-phase M-HMO. Once the pressure further increases just by 2 GPa, i.e., up to 20 GPa, a new R-HMO phase instead of the M-HMO one is stabilized. It means that the phase stability of $HgMnO_3$ is very sensitive to synthesis pressure, since high pressure can effectively tune the ionic size as well as the electronic properties. As a result, both the ilmenite-like and perovskite-like $HgMnO_3$ phases are stabilized by different pressures together with high-temperature conditions, leading to distinct magnetic properties varying from 2D to 3D.

CONCLUSION

In summary, we have succeeded in the preparation of two $HgMnO_3$ polymorphic phases under high-pressure and high-temperature conditions. One crystallizes into an ilmenite-like monoclinic phase with space group $P2_1/c$ at 18 GPa and 1473 K. The other has a perovskite-like rhombohedral structure with space group $R\bar{3}c$ at 20 GPa and 1473 K. The charge state of Mn in these two phases is an invariable +4. The magnetic MnO_6 octahedra are spatially isolated by Hg atoms along the *a*-axis in the monoclinic phase, leading to the formation of 2D MnO_6 arrangement in *bc* plane. As a result, typical 2D magnetic properties are found to occur in this phase as demonstrated by a broad hump in the magnetic susceptibility around 60 K followed by a drastic drop at a lower long-range antiferromagnetic ordering temperature $T_N \sim 32$ K. On the other hand, the magnetic MnO_6 octahedra in the rhombohedral phase of $HgMnO_3$ are connected with each other by sharing corners in 3D space, giving rise to antiferromagnetic phase transition at a higher $T_N \sim 60$ K. Although the whole family of $A^{2+}Mn^{4+}O_3$ (A = Mg, Hg, Ca, Sr, Pb, Ba) changes the structure from ilmenite (A = Mg) to perovskite, the tolerance factor and normalized average unit cell volume display linear relationships with ionic radius. The current $HgMnO_3$ provides a good example to study the geometrical dependence of the magnetism in polymorphic phases with isoelectronic configurations.

AUTHOR INFORMATION

Corresponding Author

Youwen Long − *Beijing National Laboratory for Condensed Matter Physics, Institute of Physics, Chinese Academy of Sciences, Beijing 100190, China; School of Physical Sciences, University of Chinese Academy of Sciences, Beijing 100049, China; Songshan Lake Materials Laboratory, Dongguan, Guangdong 523808, China;* orcid.org/0000-0002-8587-7818; Email: ywlong@iphy.ac.cn

Authors

Bowen Zhou − *Beijing National Laboratory for Condensed Matter Physics, Institute of Physics, Chinese Academy of Sciences, Beijing 100190, China; School of Physical Sciences, University of Chinese Academy of Sciences, Beijing 100049, China*

Shijun Qin − *Beijing National Laboratory for Condensed Matter Physics, Institute of Physics, Chinese Academy of Sciences, Beijing 100190, China; School of Physical Sciences, University of Chinese Academy of Sciences, Beijing 100049, China*

Teng Ma − *Beijing National Laboratory for Condensed Matter Physics, Institute of Physics, Chinese Academy of Sciences, Beijing 100190, China*

Xubin Ye − *Beijing National Laboratory for Condensed Matter Physics, Institute of Physics, Chinese Academy of Sciences, Beijing 100190, China; School of Physical Sciences, University of Chinese Academy of Sciences, Beijing 100049, China*

Jia Guo − *Beijing National Laboratory for Condensed Matter Physics, Institute of Physics, Chinese Academy of Sciences, Beijing 100190, China; School of Physical Sciences, University of Chinese Academy of Sciences, Beijing 100049, China*

Xiaohui Yu − *Beijing National Laboratory for Condensed Matter Physics, Institute of Physics, Chinese Academy of Sciences, Beijing 100190, China; School of Physical Sciences, University of Chinese Academy of Sciences, Beijing 100049, China*

Hong-Ji Lin − *National Synchrotron Radiation Research Center, Hsinchu 30076, Taiwan, ROC*

Chien-Te Chen − *National Synchrotron Radiation Research Center, Hsinchu 30076, Taiwan, ROC*

Zhiwei Hu − *Max Planck Institute for Chemical Physics of Solids, Dresden 01187, Germany*

Liu-Hao Tjeng − *Max Planck Institute for Chemical Physics of Solids, Dresden 01187, Germany*

Guanghui Zhou − *Department of Physics and Synergetic Innovation Center for Quantum Effects and Applications of Hunan, Hunan Normal University, Changsha 410081, China*

Cheng Dong − *Beijing National Laboratory for Condensed Matter Physics, Institute of Physics, Chinese Academy of Sciences, Beijing 100190, China; School of Physical Sciences, University of Chinese Academy of Sciences, Beijing 100049, China*

Complete contact information is available at:
https://pubs.acs.org/10.1021/acs.inorgchem.9b03551

Notes

The authors declare no competing financial interest.

ACKNOWLEDGMENTS

This work was supported by the National Key R&D Program of China (2018YFE0103200, 2018YFA0305700), the National Natural Science Foundation of China (11934017, 51772324, 11921004, 11574378), and the Chinese Academy of Sciences (QYZDB-SSW-SLH013, GJHZ1773, YZ201555). We acknowledge the support from the Max Planck−POSTECH−Hsinchu center for complex phase materials.

REFERENCES

(1) Schiffer, P.; Ramirez, A. P.; Bao, W.; Cheong, S. W. Low temperature magnetoresistance and the magnetic phase diagram of $La_{1-x}Ca_xMnO_3$. *Phys. Rev. Lett.* **1995**, *75*, 3336−3339.

(2) Urushibara, A.; Moritomo, Y.; Arima, T.; Asamitsu, A.; Kido, G.; Tokura, Y. Insulator-metal transition and giant magnetoresistance in $La_{1-x}Sr_xMnO_3$. *Phys. Rev. B: Condens. Matter Mater. Phys.* **1995**, *51*, 14103−14109.

(3) Mizokawa, T.; Fujimori, A. Spin, charge, and orbital ordering in Mn perovskite oxides studied by model Hartree-Fock calculations. *Phys. Rev. B: Condens. Matter Mater. Phys.* **1997**, *56*, 493−496.

(4) Kimura, T.; Kawamoto, S.; Yamada, I.; Azuma, M.; Takano, M.; Tokura, Y. Magnetocapacitance effect in multiferroic$BiMnO_3$. *Phys. Rev. B: Condens. Matter Mater. Phys.* **2003**, *67*, 180401.

(5) Imada, M.; Fujimori, A.; Tokura, Y. Metal-insulator transitions. *Rev. Mod. Phys.* **1998**, *70*, 1039−1263.

(6) Zhou, L.; Dai, J.; Chai, Y.; Zhang, H.; Dong, S.; Cao, H.; Calder, S.; Yin, Y.; Wang, X.; Shen, X.; Liu, Z.; Saito, T.; Shimakawa, Y.; Hojo, H.; Ikuhara, Y.; Azuma, M.; Hu, Z.; Sun, Y.; Jin, C.; Long, Y. Realization of large electric polarization and strong magnetoelectric coupling in $BiMn_3Cr_4O_{12}$. *Adv. Mater.* **2017**, *29*, 1703435.

(7) Wang, X.; Chai, Y.; Zhou, L.; Cao, H.; Cruz, C. D.; Yang, J.; Dai, J.; Yin, Y.; Yuan, Z.; Zhang, S.; Yu, R.; Azuma, M.; Shimakawa, Y.; Zhang, H.; Dong, S.; Sun, Y.; Jin, C.; Long, Y. Observation of magnetoelectric multiferroicity in a cubic perovskite system: $LaMn_3Cr_4O_{12}$. *Phys. Rev. Lett.* **2015**, *115*, 087601.

(8) Salamon, M. B.; Jaime, M. The physics of manganites: Structure and transport. *Rev. Mod. Phys.* **2001**, *73*, 583−628.

(9) Belik, A. A.; Matsushita, Y.; Katsuya, Y.; Tanaka, M.; Kolodiazhnyi, T.; Isobe, M.; Takayama-Muromachi, E. Crystal structure and magnetic properties of 6H-$SrMnO_3$. *Phys. Rev. B: Condens. Matter Mater. Phys.* **2011**, *84*, 94438.

(10) Søndenå, R.; Stølen, S.; Ravindran, P.; Grande, T. Heat capacity and lattice dynamics of cubic and hexagonal$SrMnO_3$: Calorimetry and density functional theory simulations. *Phys. Rev. B: Condens. Matter Mater. Phys.* **2007**, *75*, 214307.

(11) Chamberland, B. L.; Sleight, A. W.; Weiher, J. F. Preparation and characterization of $BaMnO_3$ and $SrMnO_3$ polytypes. *J. Solid State Chem.* **1970**, *1*, 506−511.

(12) Cussen, E. J.; Battle, P. D. Crystal and magnetic structures of 2H BaMnO3. *Chem. Mater.* **2000**, *12*, 831−838.

(13) Syono, Y.; Akimoto, S.-i.; Kohn, K. Structure relations of hexagonal perovskite-like compounds ABX_3 at high pressure. *J. Phys. Soc. Jpn.* **1969**, *26*, 993−999.

(14) Oka, K.; Azuma, M.; Hirai, S.; Belik, A. A.; Kojitani, H.; Akaogi, M.; Takano, M.; Shimakawa, Y. Pressure-induced transformation of 6H hexagonal to 3C perovskite structure in $PbMnO_3$. *Inorg. Chem.* **2009**, *48*, 2285−2288.

(15) Poeppelmeier, K. R.; Leonowicz, M. E.; Scanlon, J. C.; Longo, J. M.; Yelon, W. B. Structure determination of $CaMnO_3$ and $CaMnO_{2.5}$ by X-ray and neutron methods. *J. Solid State Chem.* **1982**, *45*, 71−79.

(16) Fava, F. F.; D'Arco, P.; Orlando, R.; Dovesi, R. A quantum mechanical investigation of the electronic and magnetic properties of perovskite. *J. Phys.: Condens. Matter* **1997**, *9*, 489−498.

(17) Chamberland, B. L.; Sleight, A. W.; Weiher, J. F. Preparation and characterization of $MgMnO_3$ and $ZnMnO_3$. *J. Solid State Chem.* **1970**, *1*, 512−514.

(18) Shannon, R. D. *Acta Crystallogr., Sect. A: Cryst. Phys., Diffr., Theor. Gen. Crystallogr.* **1976**, *32*, 751−767.

(19) Sleight, A. W.; Prewitt, C. T. High-pressure $HgTiO_3$ and $HgPbO_3$: Preparation, characterization, and structure. *J. Solid State Chem.* **1973**, *6*, 509−512.

(20) Chen, J.; Matsushita, Y.; Kolodiazhnyi, T.; Belik, A. A.; Tsujimoto, Y.; Katsuya, Y.; Tanaka, M.; Su, Y.; Shi, Y.; Yamaura, K. High-pressure synthesis, crystal structure, and semimetallic properties of $HgPbO_3$. *Inorg. Chem.* **2018**, *57*, 7601−7609.

(21) Inaguma, Y.; Tanaka, K.; Tsuchiya, T.; Mori, D.; Katsumata, T.; Ohba, T.; Hiraki, K.; Takahashi, T.; Saitoh, H. Synthesis, structural transformation, thermal stability, valence state, and magnetic and electronic properties of $PbNiO_3$ with perovskite- and $LiNbO_3$-type structures. *J. Am. Chem. Soc.* **2011**, *133*, 16920−16929.

(22) Altomare, A.; Cuocci, C.; Giacovazzo, C.; Moliterni, A.; Rizzi, R.; Corriero, N.; Falcicchio, A. EXPO2013: a kit of tools for phasing crystal structures from powder data. *J. Appl. Crystallogr.* **2013**, *46*, 1231−1235.

(23) Rodríguez-Carvajal, J. Recent advances in magnetic structure determination by neutron powder diffraction. *Phys. B* **1993**, *192*, 55−69.

(24) Burnus, T.; Hu, Z.; Hsieh, H. H.; Joly, V. L. J.; Joy, P. A.; Haverkort, M. W.; Wu, H.; Tanaka, A.; Lin, H. J.; Chen, C. T.; Tjeng, L. H. Local electronic structure and magnetic properties of$LaMn_{0.5}Co_{0.5}O_3$ studied by x-ray absorption and magnetic circular dichroism spectroscopy. *Phys. Rev. B: Condens. Matter Mater. Phys.* **2008**, *77*, 125124.

(25) Hossain, M. A.; Hu, Z.; Haverkort, M. W.; Burnus, T.; Chang, C. F.; Klein, S.; Denlinger, J. D.; Lin, H.-J.; Chen, C. T.; Mathieu, R.; Kaneko, Y.; Tokura, Y.; Satow, S.; Yoshida, Y.; Takagi, H.; Tanaka, A.; Elfimov, I. S.; Sawatzky, G. A.; Tjeng, L. H.; Damascelli, A. Crystal-field level inversion in lightly Mn-doped $Sr_3Ru_2O_7$. *Phys. Rev. Lett.* **2008**, *101*, 016404.

(26) Chang, C. F.; Hu, Z.; Wu, H.; Burnus, T.; Hollmann, N.; Benomar, M.; Lorenz, T.; Tanaka, A.; Lin, H. J.; Hsieh, H. H.; Chen, C. T.; Tjeng, L. H. Spin blockade, orbital occupation, and charge ordering in $La_{1.5}Sr_{0.5}CoO_4$. *Phys. Rev. Lett.* **2009**, *102*, 116401.

(27) Wu, H.; Burnus, T.; Hu, Z.; Martin, C.; Maignan, A.; Cezar, J. C.; Tanaka, A.; Brookes, N. B.; Khomskii, D. I.; Tjeng, L. H. Ising magnetism and ferroelectricity in Ca_3CoMnO_6. *Phys. Rev. Lett.* **2009**, *102*, 026404.

(28) Clement, R.; Girerd, J.; Morgenstern-Badarau, I. Dramatic modification of the magnetic properties of lamellar manganese trithiophosphonite ($MnPS_3$) upon intercalation. *Inorg. Chem.* **1980**, *19*, 2852−2854.

(29) Zhou, C.; Wang, J.; Liu, X.; Chen, F.; Di, Y.; Gao, S.; Shi, Q. Magnetic and thermodynamic properties of α, β, γ and δ-MnO2. *New J. Chem.* **2018**, *42*, 8400−8407.

(30) Fawcett, I. D.; Sunstrom; Greenblatt, M.; Croft, M.; Ramanujachary, K. V. Structure, magnetism, and properties of ruddlesden-popper calcium manganates prepared from citrate gels. *Chem. Mater.* **1998**, *10*, 3643−3651.

(31) Zhang, H.; Li, N.; Li, K.; Xue, D. F. Structural stability and formability of ABO_3-type perovskite compounds. *Acta Crystallogr., Sect. B: Struct. Sci.* **2007**, *63*, 812−818.

(32) Li, C.; Soh, K. C. K.; Wu, P. Formability of ABO_3 perovskites. *J. Alloys Compd.* **2004**, *372*, 40−48.

(33) Goldschmidt, V. M. The laws of crystal chemistry. *Naturwissenschaften* **1926**, *14*, 477−485.

(34) Rodriguez-Martinez, L. M.; Attfield, J. P. Cation disorder and size effects in magnetoresistive manganese oxide perovskites. *Phys. Rev. B: Condens. Matter Mater. Phys.* **1996**, *54*, 15622−15625.

(35) Troyanchuk, I. O.; Derkachenko, V. N.; Shapovalova, E. F. High-pressure synthesis and properties of manganates with ilmenite structure. *Cryst. Res. Technol.* **1992**, *27*, 593−598.

(36) Brown, I. D.; Altermatt, D. Bond-valence parameters obtained from a systematic analysis of the inorganic crystal structure database. *Acta Crystallogr., Sect. B: Struct. Sci.* **1985**, *41*, 244−247.